nature chemistry

ARTICLES

PUBLISHED ONLINE: 23 MAY 2010 | DOI: 10.1038/NCHEM.670

Synthesis of a metal oxide with a room-temperature photoreversible phase transition

Shin-ichi Ohkoshi[1]*, Yoshihide Tsunobuchi[1], Tomoyuki Matsuda[1], Kazuhito Hashimoto[2], Asuka Namai[1], Fumiyoshi Hakoe[1] and Hiroko Tokoro[1]

Photoinduced phase-transition materials, such as chalcogenides, spin-crossover complexes, photochromic organic compounds and charge-transfer materials, are of interest because of their application to optical data storage. Here we report a photoreversible metal–semiconductor phase transition at room temperature with a unique phase of Ti_3O_5, λ-Ti_3O_5. λ-Ti_3O_5 nanocrystals are made by the combination of reverse-micelle and sol–gel techniques. Thermodynamic analysis suggests that the photoinduced phase transition originates from a particular state of λ-Ti_3O_5 trapped at a thermodynamic local energy minimum. Light irradiation causes reversible switching between this trapped state (λ-Ti_3O_5) and the other energy-minimum state (β-Ti_3O_5), both of which are persistent phases. This is the first demonstration of a photorewritable phenomenon at room temperature in a metal oxide. λ-Ti_3O_5 satisfies the operation conditions required for a practical optical storage system (operational temperature, writing data by short wavelength light and the appropriate threshold laser power).

High-density optical memory devices based on blue-laser irradiation are now being developed. In such optical memory devices, phase-change materials, such as chalcogenides, are used as the rewritable recording material. Coupled with such optoelectronic applications, studies of photoinduced phase transitions were developed aggressively. To date, several types of photoinduced phase-transition phenomena have been reported; for example, a light-induced crystalline–amorphous transformation in a chalcogenide[1,2], a light-induced excited spin-state trapping in a spin-crossover complex[3–8], a light-induced structural transformation in a photochromic compound[9–12], a light-induced charge transfer in a donor–acceptor stacked molecule[13,14], a cyanobridged metal assembly[15–21] or a perovskite manganite[22,23]. Herein we report a unique phase of titanium oxide, λ-Ti_3O_5. λ-Ti_3O_5 shows a reversible, photoinduced metal–semiconductor phase transition between λ-Ti_3O_5 and β-Ti_3O_5 at room temperature. This is the first observation of a metal oxide with a photoinduced phase transition at room temperature. In this paper we report the synthesis and crystal structure of λ-Ti_3O_5, the magnetic, electrical and optical properties and electronic structure of λ-Ti_3O_5, the photoreversible phase transition at room temperature and a thermodynamic interpretation of the photoinduced phase transition.

Results and discussion

A unique phase of titanium oxide, λ-Ti_3O_5, was obtained in two morphological types by different synthetic methods: one type was a λ-Ti_3O_5 nanocrystal in a SiO_2 matrix and the other a flake form of λ-Ti_3O_5 assembled by nanocrystals. The former was obtained by a combination of reverse-micelle and sol–gel techniques (Fig. 1a and the Methods section). The transmission electron microscope (TEM) image of λ-Ti_3O_5–SiO_2 shows cubic-shaped Ti_3O_5 nanocrystals with an average size of 21 ± 11 nm dispersed in a SiO_2 matrix (Fig. 1b). Moreover, the X-ray diffraction (XRD) pattern indicates a crystal structure of $C2/m$ (Fig. 2a,b), which does not correspond to any reported crystal structures of Ti_3O_5 (α-, β-, γ- and δ-phases)[24–26]. Details of the crystal structure of λ-Ti_3O_5 nanocrystals in SiO_2 are reported in Supplementary Table S1. In contrast, the flake form of λ-Ti_3O_5 was prepared by calcinating the anatase form of the TiO_2 nanoparticles under hydrogen at 1,200 °C. The TEM image shows that the flake (2 ± 0.5 μm) was assembled from 25 ± 15 nm nanocrystals (Supplementary Fig. S1). The XRD pattern of the sample at room temperature corresponded to the aforementioned λ-Ti_3O_5 in SiO_2, and the Rietveld analysis showed a monoclinic structure ($C2/m$) (Supplementary Figs S2 and S3). Variable-temperature XRD measurements demonstrated that, as the temperature increased, the diffraction peaks of λ-Ti_3O_5 continuously changed to α-Ti_3O_5 peaks with a crystal structure of $Cmcm$, for example (2 0 −3) and (2 0 3) of λ-Ti_3O_5 → (0 2 3) of α-Ti_3O_5 (Fig. 2c). Furthermore, heating the sample to 640 K and then cooling to 300 K caused α-Ti_3O_5 to return to λ-Ti_3O_5. The details of synthesis and crystal structure of the flake form λ-Ti_3O_5 are reported in the Methods section, Supplementary Fig. S4 and Table S2. Differential scanning calorimetry (DSC) measurements did not exhibit a meaningful peak (Fig. 2d), which differs greatly from the first-order phase transition between β-Ti_3O_5 and α-Ti_3O_5 in a conventional, large Ti_3O_5 crystal[27–31]. Hence, the phase transition between λ-Ti_3O_5 and α-Ti_3O_5 is classified as a second-order phase transition.

Figure 3a shows the magnetic susceptibility (χ) versus temperature (T) curve of the flake form λ-Ti_3O_5 as well as the χ versus T curve of a conventional large crystal of Ti_3O_5. λ-Ti_3O_5 has χ values around 2×10^{-4} e.m.u. per Ti atom throughout the entire measured temperature region, which suggests that λ-Ti_3O_5 is a Pauli paramagnet because of metallic conduction. Spin–orbital coupling on the Ti^{3+} ion can explain the gradual decrease below 150 K, but the rapid increase below 30 K is attributed to a small amount of Curie paramagnetism (about 0.1%), which may be caused by defects in the material. The λ-Ti_3O_5–SiO_2 sample exhibited the same type of χ versus T curve (Supplementary Fig. S5). The electric current versus voltage curve using atomic force microscopy in the contact mode had an electrical conductivity (σ) value of about 30 S cm^{-1}, which indicates that λ-Ti_3O_5 is a near-metallic conductor. Additionally, both the ultraviolet–visible and infrared reflectance spectra indicate that λ-Ti_3O_5

[1]Department of Chemistry, School of Science, The University of Tokyo, 7-3-1 Hongo, Bunkyo-ku, Tokyo 113-0033, Japan, [2]Department of Applied Chemistry, School of Engineering, The University of Tokyo, 7-3-1 Hongo, Bunkyo-ku, Tokyo 113-8656, Japan. *e-mail: ohkoshi@chem.s.u-tokyo.ac.jp

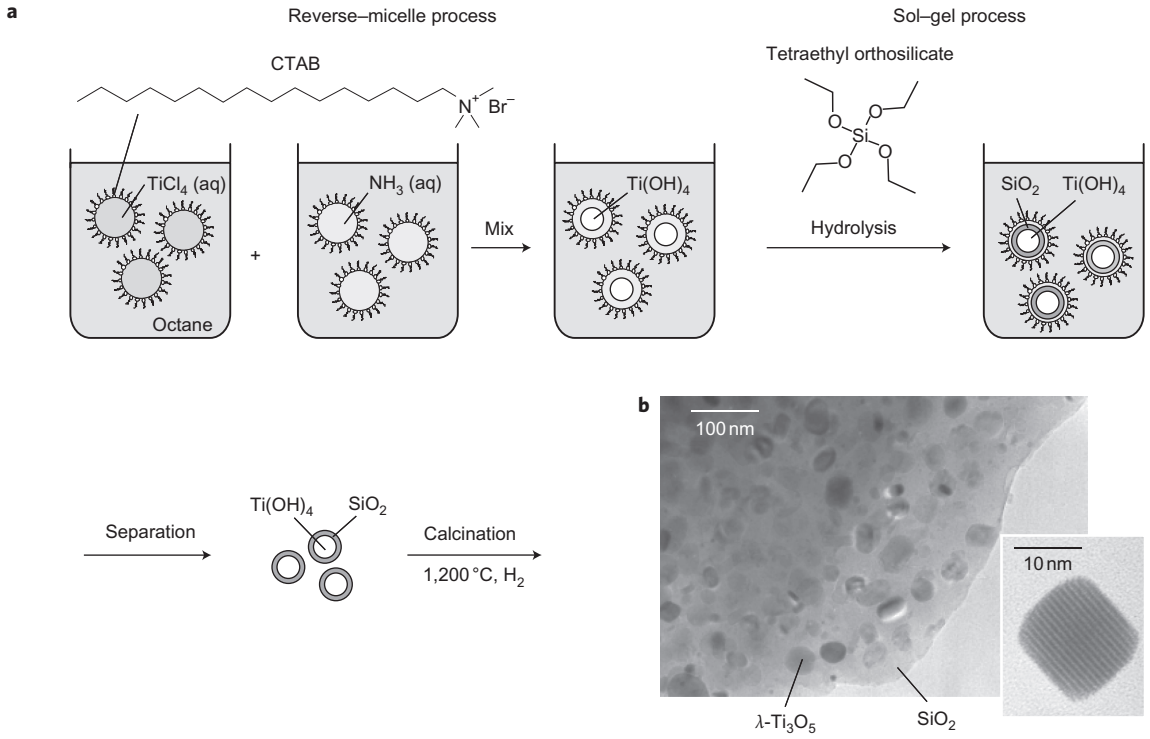

Figure 1 | Synthesis procedure for λ-Ti_3O_5 nanocrystals in a SiO_2 matrix. a, A combination of reverse-micelle and sol-gel techniques is used to synthesize the λ-Ti_3O_5 nanocrystals in a SiO_2 matrix. **b,** TEM image of λ-Ti_3O_5 nanocrystals in a SiO_2 matrix. The inset is an enlarged image that shows the lattice planes.

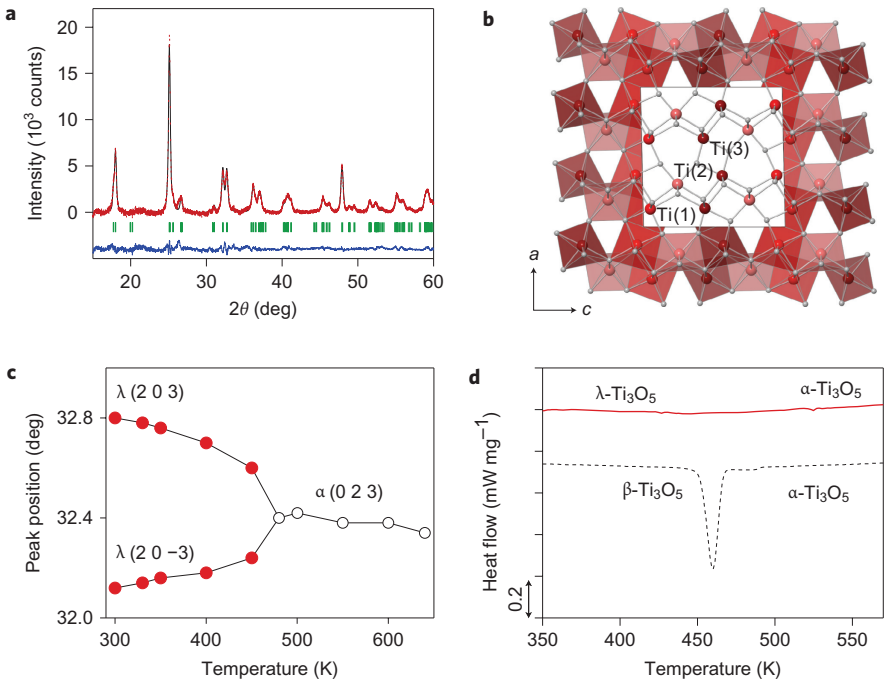

Figure 2 | Formation and crystal structure of λ-Ti_3O_5. a, Powder XRD pattern of λ-Ti_3O_5 nanocrystals in SiO_2. Broad deviation of the baseline caused by amorphous SiO_2 is eliminated. Red dots, black lines and blue lines are the observed patterns, calculated patterns and their differences, respectively, and green bars represent the calculated positions of the Bragg reflections of λ-Ti_3O_5. **b**, Crystal structure for λ-Ti_3O_5 (monoclinic $C2/m$). Red, light red, deep red and grey balls represent Ti(1), Ti(2), Ti(3) and O atoms, respectively, and TiO_6 units are drawn as polyhedra. The central square without polyhedra represents the unit cell. **c**, Peak position versus temperature graph of the XRD pattern in the angle range 32.0–33.0° for the flake form λ-Ti_3O_5. **d**, DSC charts of the flake form λ-Ti_3O_5 (red line) and conventional crystal Ti_3O_5 (dashed black line) with increasing temperature.

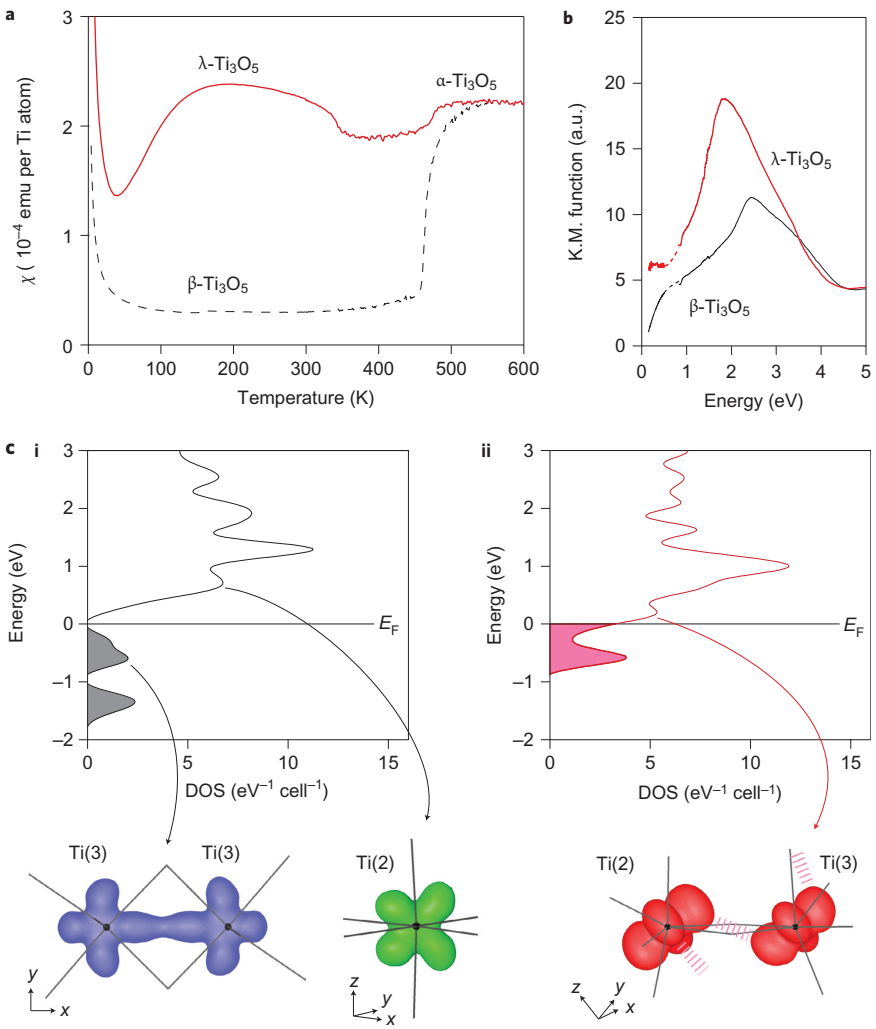

Figure 3 | Magnetic and optical properties, and electronic structures of λ-Ti_3O_5. **a**, χ versus T graph of the flake form λ-Ti_3O_5 (red line) and single-crystal β-Ti_3O_5 (dashed black line) under an external field of 0.5 T. **b,** Optical absorption spectra of the flake form λ-Ti_3O_5 (red line) and β-Ti_3O_5 (black line) in the ultraviolet-visible and infrared regions. K.M. = Kubelka–Munk transformation. **c,** Band structures of β-Ti_3O_5 and λ-Ti_3O_5 using VASP, showing the DOS around the Fermi level (E_F) for β-Ti_3O_5 (**i**) and λ-Ti_3O_5 (**ii**). Below these are the electron-density maps around the Fermi level.

possesses metallic absorption over ultraviolet and infrared wavelengths (Fig. 3b). In contrast, the impedance measurement and reflectance spectra suggest that β-Ti_3O_5 is a semiconductor with $\sigma = 3 \times 10^{-2}$ S cm^{-1} and a band gap of 0.14 eV.

The empirical relationship between the bond length and valence states[32] gives estimated valence states for Ti(1), Ti(2) and Ti(3) in λ-Ti_3O_5 of +3.37, +3.20 and +3.53, respectively. These valence states are close to $Ti^{10/3+}$, which indicates that λ-Ti_3O_5 is a charge-delocalized system, consistent with λ-Ti_3O_5 being a metallic conductor. The electronic structure of λ-Ti_3O_5 is close to that of α-Ti_3O_5. In contrast, the valence states of Ti(1), Ti(2) and Ti(3) in β-Ti_3O_5 are +3.00, +3.79 and +3.32, respectively, which are close to the valence states for a charge-localized system of Ti^{3+}–$Ti^{11/3+}$–$Ti^{10/3+}$. The band structures of β-Ti_3O_5 and λ-Ti_3O_5 were calculated from first principles using the Vienna *ab initio* simulation package (VASP)[33,34]. The bands near the Fermi level were consistent with the t_{2g} orbitals of the octahedral 3*d* orbital of Ti ions. The t_{2g} orbitals were split by coupling with neighbouring Ti ions. In β-Ti_3O_5, the valence band was formed by a bipolaron (a pair of polarons with no spin) of Ti(3)–Ti(3) caused by σ-type bonding of d_{xy} orbitals on Ti(3), and its band was located at –0.60 eV. The conduction band consisted mainly of an empty d_{xz} orbital on Ti(2) at +0.71 eV (Fig. 3ci). The energy between these two bands (that is, the bandgap) was estimated to be 0.13 eV, consistent with the 0.14 eV observed in the optical reflection spectrum. In λ-Ti_3O_5, slipped π-stacking (like a zigzag chain) between the d_{xy} orbital on Ti(2) and the d_{xy} orbital on Ti(3) formed. The band was located at the position of the Fermi level (Fig. 3cii), and resulted in λ-Ti_3O_5 becoming a metallic conductor. As for the Ti(1)–Ti(1) dimer, its band was located at –1.35 eV in β-Ti_3O_5 and at –0.58 eV in λ-Ti_3O_5. The details of the band structures and density of states (DOS) plots are reported in the Methods section and Supplementary Figs S6 and S7.

When the flake form λ-Ti_3O_5 was irradiated with 532 nm nanosecond laser light (6 ns, five shots, 1.5×10^{-5} mJ μm^{-2} pulse^{-1}) at room temperature, the irradiated area changed from black to brown (Fig. 4a,b, Supplementary Movie S1). Subsequent irradiation with 410 nm laser light (8×10^{-3} mW μm^{-2}) caused the irradiated spots to return to black (Fig. 4c,d). Alternatively, repeated irradiation at 532 nm and 410 nm induced these colour changes (Fig. 4e–i). The XRD pattern showed that the brown area was the β-phase (monoclinic structure $C2/m$). Hence, the change from black to brown was caused by the transition from λ-Ti_3O_5 to β-Ti_3O_5, and the converse was caused by the transition from the β-Ti_3O_5 to λ-Ti_3O_5. Furthermore, irradiation with different nanosecond-pulsed laser lights, 355 or 1,064 nm, caused a similar phase transition.

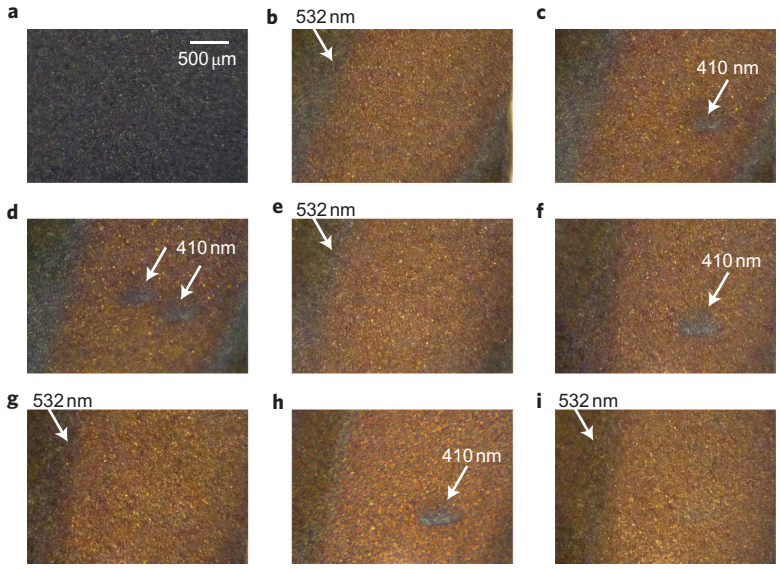

Figure 4 | Reversible photoinduced phase transition in λ-Ti_3O_5. a–i, Photographs of λ-Ti_3O_5 at irradiations of 532 nm and 410 nm laser lights. When the flake form λ-Ti_3O_5 was irradiated with 532 nm nanosecond-pulsed laser light at room temperature, the irradiated area changed from black (**a**) to brown (**b**). Subsequently, on irradiating with 410 nm laser light the spots returned from brown to black (**c**,**d**). Photoinduced colour changes were observed repeatedly by alternating 532 nm and 410 nm laser-light irradiation (**e–i**).

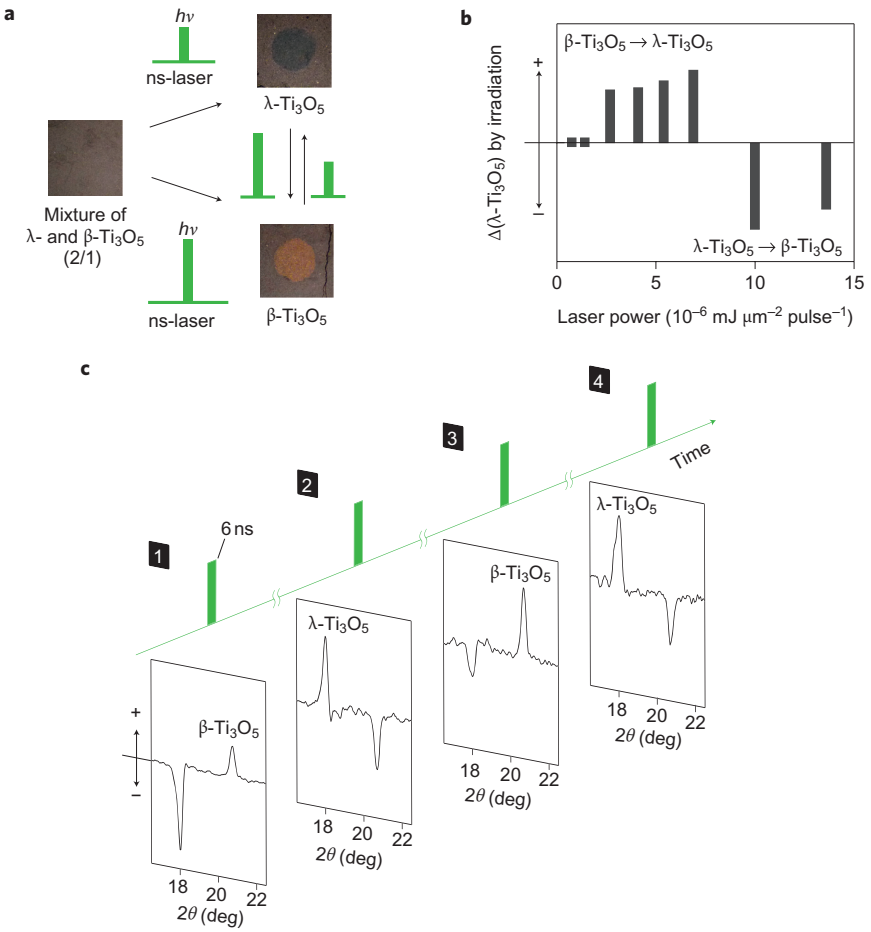

Figure 5 | Phase transition between λ-Ti_3O_5 and β-Ti_3O_5 induced by one-shot laser pulses. a, A mixed sample of λ- and β-phases (λ/β = 2/1) was irradiated with 532 nm pulsed laser light at various laser-power densities. **b**, The change in amount of λ-Ti_3O_5 from the ratio 2/1, Δ(λ-Ti_3O_5), versus laser-power density. Clear thresholds for laser-power densities were observed. **c,** Difference XRD patterns of the alternating phase transition between λ-Ti_3O_5 and β-Ti_3O_5 by irradiation of pulsed-laser (532 nm, 6 ns) shots at room temperature.

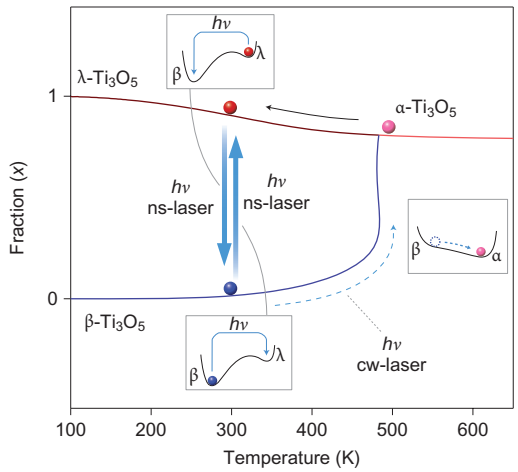

Figure 6 | Mechanism of the photoinduced phase transition in λ-Ti_3O_5. Thermally populated phase versus temperature curves are based on the *G* versus *x* plots for Ti_3O_5 nanocrystals using the observed ΔH (= 4.8 kJ mol^{-1}) and ΔS (= 10.4 J K^{-1} mol^{-1}) values and assuming γ = 9.0 kJ mol^{-1}. Red, pink and blue lines indicate λ-Ti_3O_5, α-Ti_3O_5 and β-Ti_3O_5, respectively. The photoinduced phase transition from λ-Ti_3O_5 to β-Ti_3O_5 is attributed to the phase transition from a metastable phase to a true stable phase (blue arrow pointing downwards and top inset). In the reverse photoinduced phase transition from β-Ti_3O_5 to λ-Ti_3O_5, the transition by the nanosecond (ns)-pulsed laser-light irradiation is direct (blue arrow pointing upwards and middle inset) or it thermally transits through α-Ti_3O_5 to give to λ-Ti_3O_5 (that is, β-Ti_3O_5 → α-Ti_3O_5 → λ-Ti_3O_5) by continuous wave (cw) laser-light irradiation (dotted blue arrow and bottom inset).

To investigate the threshold value of nanosecond laser power, a mixed sample of λ-Ti_3O_5 and β-Ti_3O_5 (ratio of 2/1) was irradiated with 532 nm pulsed laser light (one shot) at various laser-power densities. As shown in Fig. 5a,b, the threshold laser-power of β-Ti_3O_5 → λ-Ti_3O_5 was 2.7×10^{-6} mJ μm^{-2} and, conversely, that of λ-Ti_3O_5 → β-Ti_3O_5 was above 6.9×10^{-6} mJ μm^{-2}. The existence of clear thresholds with the laser-power density indicates cooperative interaction between photoexcited sites and neighbouring sites. Such a threshold is important for long-lasting memory in recording storage media. The observed threshold values of the laser-power densities used are the same order as those used on digital versatile discs[35,36]. Based on this knowledge, using XRD we demonstrated alternating switching between λ-Ti_3O_5 and β-Ti_3O_5 induced by one-shot, nanosecond-pulsed, laser-light irradiation (532 nm, 6 ns, 7×10^{-6} mJ μm^{-2} pulse^{-1}) (Fig. 5c).

To understand the mechanism of the observed photoinduced phase transition, the thermodynamic energy of Ti_3O_5 was calculated using the Slichter and Drickamer mean-field model (see Methods section)[37]. The first-order phase transition between β-Ti_3O_5 and α-Ti_3O_5 on a conventional large-crystal Ti_3O_5 is regarded as a metal–semiconductor phase transition between charge-localized (Ti^{3+}–$Ti^{11/3+}$–$Ti^{10/3+}$) and charge-delocalized ($Ti^{10/3+}$)$_3$ systems. Also, the metal–semiconductor phase transition between β-Ti_3O_5 and α-Ti_3O_5 for conventional Ti_3O_5 was reproduced, as shown in Supplementary Fig. S8. In contrast, to analyse the phase transition between λ-Ti_3O_5 and α-Ti_3O_5, the thermodynamic parameters of the phase transition in a Ti_3O_5 nanocrystal are necessary, but unknown. In this work, λ-Ti_3O_5 nanocrystals showed a pressure-induced phase transition from λ-Ti_3O_5 to β-Ti_3O_5. That this β-Ti_3O_5 nanocrystal was produced by an external pressure indicates that the transition enthalpy (ΔH) from β-Ti_3O_5 to α-Ti_3O_5 is small and caused by the surface energy of the nanocrystal form. The details of the pressure-induced phase transition and nanoscopic effect are reported in the Methods section and in Supplementary Figs S9 and S10. The observed ΔH (= 4.8 kJ mol^{-1}) and the transition entropy (ΔS) (= 10.4 J K^{-1} mol^{-1}) values were used, assuming an interaction parameter (γ) of 9.0 kJ mol^{-1}, to calculate the Gibbs free energy (*G*) versus *x* plots for Ti_3O_5 nanocrystals given by the Slichter and Drickamer model (Supplementary Fig. S11). Energy barriers exist between the charge-localized and charge-delocalized systems throughout the temperature range. Therefore, as the temperature decreases from the high calcination temperature, the system maintains a charge-delocalized state (Fig. 6, red line). This calculation supports λ-Ti_3O_5 as a metal conductor through both charge delocalization and paramagnetism, and the phase transition between λ-Ti_3O_5 and α-Ti_3O_5 is classified as a second-order phase transition. Furthermore, β-Ti_3O_5 is a true stable phase below 460 K (Fig. 6, dark blue line).

Thermodynamic analysis of λ-Ti_3O_5 suggests that the photoinduced metal–semiconductor phase transition results from the phase transition from λ-Ti_3O_5, a metastable phase thermodynamically trapped at a local energy-minimum state, to β-Ti_3O_5, a truly stable phase, by irradiation (Fig. 6, top inset). The metallic absorption allows λ-Ti_3O_5 to absorb light effectively over a wide wavelength range from ultraviolet to near-infrared, so this metal–semiconductor phase transition was observed by irradiating with 355, 532 and 1,064 nm nanosecond-pulsed laser light. The reverse photoinduced phase transition from β-Ti_3O_5 to λ-Ti_3O_5 was induced by excitation from the valence band to the conduction band on β-Ti_3O_5, and then the excited state changed directly to λ-Ti_3O_5 in the pulsed laser irradiation (Fig. 6, middle inset), or photothermally to λ-Ti_3O_5 through α-Ti_3O_5 (that is, β-Ti_3O_5 → α-Ti_3O_5 → λ-Ti_3O_5) in continuous-wave laser-light irradiation (Fig. 6, bottom inset).

Conclusion

In this paper we report a photoreversible metal–semiconductor phase transition at room temperature with a new phase of Ti_3O_5. This phenomenon originates from a particular state of λ-Ti_3O_5 trapped at thermodynamic local energy minimum. Light irradiation causes a phase transformation from this trapped state (λ-Ti_3O_5) into another energy-minimum state (β-Ti_3O_5). This is the first demonstration of a photorewritable phenomenon at room temperature in a metal oxide. λ-Ti_3O_5 satisfies the operation conditions (an operational temperature around room temperature, writing data by short wavelength, near ultraviolet light for high memory density and the appropriate threshold laser power to maintain long-term memory). Moreover, a λ-Ti_3O_5 nanocrystal is a candidate for optical storage using near-field light. Its memory density is expected to achieve 1 terabit inch^{-2} (Supplementary Fig. S12). Furthermore, Ti is environmentally benign, and the elements used to construct λ-Ti_3O_5 are very economical. Hence, λ-Ti_3O_5 is a high-performance, photoinduced phase-transition material with harmless, sustainable and economic features suitable for the next generation of optical storage media with super-high density.

Methods

Synthesis of λ-Ti_3O_5 nanocrystals in SiO_2 matrix and isolation of λ-Ti_3O_5 nanocrystals. Microemulsion systems were formed by cetyltrimethylammonium bromide (CTAB) and 1-butanol in *n*-octane with a H_2O/CTAB molar ratio of 17/1. The microemulsion, which contained an aqueous solution of $TiCl_4$ (0.50 mol dm^{-3}), was mixed (rapid stirring) with another microemulsion that contained 11 mol dm^{-3} NH_3 aqueous solution. $Si(C_2H_5O)_4$ (22 mmol) was injected into the white solution and produced a precipitate composed of $Ti(OH)_4$. The TEM image showed spherical $Ti(OH)_4$ particles (5 nm) covered by SiO_2. The precipitate was collected by centrifugation, washed with $CHCl_3$ and CH_3OH, and then heated at 1,200 °C for five hours in a hydrogen flow of 0.3 dm^{-3} min^{-1} (Fig. 1). Elemental analysis confirmed the ratio of Ti_3O_5/SiO_2 as 13/87 weight per cent. X-ray fluorescence (XRF) analysis confirmed that an impurity element did not exist (<0.1%). The isolated λ-Ti_3O_5 nanocrystals were obtained by etching the SiO_2 matrix with a KOH ethanol solution (1 mol dm^{-3}) for 24 hours at 60 °C (Supplementary Fig. S12a).

Synthesis of the neat-flake form of λ-Ti_3O_5 assembled by nanocrystals. The anatase form of the TiO_2 nanoparticles (7 nm) was calcinating under hydrogen with a flow speed of 0.3 dm^{-3} min^{-1} at 1,200 °C for two hours, which produced the flake form λ-Ti_3O_5 (Supplementary Fig. S1). XRF analysis confirmed that an impurity element did not exist (<0.1%). Inductively-coupled plasma mass spectroscopy (ICP-MS) indicated that the formula was $Ti_{3.000(63)}O_{5.000(63)}$ (calculated Ti, 64.2%; found Ti, 64.2%).

Physical measurements. Elemental analyses on the prepared samples were carried out with ICP-MS (Agilent Technologies, HP 4500) and XRF spectroscopy (SII-SEA2120L). The TEM measurements were conducted using a JEOL JEM-2000EXII and JEM-4000FXII. The morphologies of the compounds were measured with a JEOL JSM-7000F scanning electron microscope (SEM) with a 20 kV accelerating voltage. The XRD measurements were conducted with a Rigaku Ultima IV and RINT-RAPID2-CMF and Cu Kα radiation (λ = 1.5418 Å). Rietveld analyses were performed using the RIETAN-FP program[38]. Magnetic properties were measured with a superconducting quantum interference device (SQUID) magnetometer (Quantum Design, MPMS 7). The ultraviolet–visible reflectance spectra were measured with a Shimazu UV-3100 spectrometer. The infrared spectra were recorded on a JASCO FT/IR-4100 and IRT-3000 spectrometer. DSC was performed on a Rigaku DSC 8230. The electrical conductivity was measured in contact mode using an SII SPI-4000/SPA300HV atomic force microscope.

First-principal calculation using VASP. Density functional method calculations based on a plane wave were carried out for β-Ti_3O_5 and λ-Ti_3O_5 by using the *ab initio* total energy and molecular dynamics program VASP[33,34]. The wave functions and potentials of the core orbitals were replaced by the projector-augmented wave of Blöchl, and the exchange-correlation energy was calculated by the generalized gradient approximation. The DOS and band structures were calculated with an energy cut-off of 520 eV. In our calculations, we use the Coulomb interaction parameter (U) and exchange coupling (J) as $U - J = 5.0$ eV.

Slichter and Drickamer mean-field model. The Gibbs free energy (G) of the phase transition is expressed as $G = x\Delta H + \gamma x(1-x) + T(R(x \ln x + (1-x)\ln(1-x)) - x\Delta S)$, by taking G of the charge-localized system as the origin of the energies, where x is the fraction of the charge-delocalized unit $(Ti^{10/3+})_3O_5$, ΔH is the transition enthalpy, ΔS is the transition entropy, R is the gas constant and γ is an interaction parameter.

Pressure-induced phase transition from λ-Ti_3O_5 to β-Ti_3O_5. An external pressure applied to λ-Ti_3O_5 induced a phase transition. When the flake form λ-Ti_3O_5 was pressed with an external pressure of 0.3 GPa, 25% of λ-Ti_3O_5 was converted into β-Ti_3O_5 (Supplementary Fig. S9), and this sample exhibited a ΔH value from the β- to α-phase of 4.8 kJ mol^{-1} in the DSC measurement, which is smaller than that of a conventional large-crystal β-Ti_3O_5 (Supplementary Fig. S10).

Nanoscopic effect on Ti_3O_5 phase. For a nanoparticle, the contribution of the surface or interface energy perturbs the free energy ($G = H - TS$), and $G = G_B + (6V_m/d)G_S$, where G_B is the bulk free energy, G_S is the surface (or interface) free energy, V_m is the molar volume and d is the diameter of the nanoparticle. As β-Ti_3O_5 is in the low temperature phase, $G_B(\alpha) > G_B(\beta)$ in the Ti_3O_5 system. If G_S satisfies the condition $G_S(\alpha) < G_S(\beta)$, the value of $G(\beta) - G(\alpha)$ shrinks. This nanoscopic effect may contribute to the decreased ΔH value in the phase transition from β- to α-phases in a Ti_3O_5 nanocrystal. Hence, the decrease in the ΔH value in the aforementioned pressure-induced phase-transition experiment is explained by this nanoscopic effect. Such an effect was observed in Al_2O_3 (ref. 39) and Fe_2O_3 (ref. 40). A similar nanoscopic effect was observed in superionic AgI (ref. 41).

Received 30 November 2009; accepted 13 April 2010; published online 23 May 2010

References

1. Yamada, N., Ohno, E., Nishiuchi, K., Akahira, N. & Takao, M. Rapid-phase transitions of GeTe–Sb_2Te_3 pseudobinary amorphous thin films for an optical disk memory. *J. Appl. Phys.* **69,** 2849–2856 (1991).
2. Kolobov, A. V. *et al.* Understanding the phase-change mechanism of rewritable optical media. *Nature Mater.* **3,** 703–708 (2004).
3. Gütlich, P., Hauser, A. & Spiering, H. Thermal and optical switching of iron(II) complexes *Angew. Chem. Int. Ed. Engl.* **33,** 2024–2054 (1994).
4. Nasu, K. *Relaxations of Excited States and Photo-Induced Structural Phase Transitions* (Springer, 1997).
5. Kahn, O. & Martinez, C. J. Spin-transition polymers: from molecular materials toward memory devices. *Science* **279,** 44–48 (1998).
6. Decurtins, S., Gütlich, P., Köhler, C.P., Spiering, H. & Hauser, A. Light-induced excited spin state trapping in a transition-metal complex: the hexa-1-propyltetrazole-iron(II) tetrafluoroborate spin-crossover system *Chem. Phys. Lett.* **105,** 1–4 (1984).
7. Létard, J. F. *et al.* Light induced excited pair spin state in an iron(II) binuclear spin-crossover compound. *J. Am. Chem. Soc.* **121,** 10630–10631 (1999).
8. Varret, F. *et al.* Thermally induced dilution of the photo-induced magnetic state of Prussian Blue analogues. *Mol. Cryst. Liq. Cryst.* **379,** 333–340 (2002).
9. Dürr, H. & Bouas-Laurent, H. *Photochromism: Molecules and Systems* (Elsevier, 1990).
10. Aktsipetrov, O. A., Fedyanin, A. A., Melnikov, A. V., Mishina, E. D. & Murzina, T. V. Second harmonic generation as a nondestructive readout of optical (photo(electro)chromic and magnetic) memories. *Jpn J. Appl. Phys.* **37,** 122–127 (1998).
11. Irie, M., Fukaminato, T., Sasaki, T., Tamai, N. & Kawai, T. Organic chemistry: a digital fluorescent molecular photoswitch. *Nature* **420,** 759–760 (2002).
12. Habuchi, S. *et al.* Reversible single-molecule photoswitching in the GFP-like fluorescent protein Dronpa. *Proc. Natl Acad. Sci. USA* **102,** 9511–9516 (2005).
13. Koshihara, S., Tokura, Y., Mitani, T., Saito, G. & Koda, T. Photoinduced valence instability in the organic molecular compound tetrathisfulvalence-p-chloranil (TTF-CA). *Phys. Rev. B* **42,** 6853–6856 (1990).
14. Collet, E. *et al.* Laser-induced ferroelectric structural order in an organic charge-transfer crystal. *Science* **300,** 612–615 (2003).
15. Ohkoshi, S. & Hashimoto, K. Photo-magnetic and magneto-optical effects of functionalized metal polycyanides. *J. Photochem. Photobiol. C* **2,** 71–88 (2001).
16. Verdaguer, M. Molecular electronics emerges from molecular magnetism. *Science* **272,** 698–699 (1996).
17. Ohkoshi, S. *et al.* Photoinduced magnetic pole inversion in a ferro–ferrimagnet: $(Fe^{II}_{0.40}Mn^{II}_{0.60})_{1.5}Cr^{III}(CN)_6$. *Appl. Phys. Lett.* **70,** 1040–1042 (1997).
18. Herrera, J. M. *et al.* Reversible photoinduced magnetic properties in the heptanuclear complex $[Mo^{IV}(CN)_2(CN–CuL)_6]^{8+}$: a photomagnetic high-spin molecule. *Angew. Chem. Int. Ed.* **43,** 5468–5471 (2004).
19. Dei, A. Photomagnetic effects in polycyanometallate compounds: an intriguing future chemically based technology? *Angew. Chem. Int. Ed.* **44,** 1160–1163 (2005).
20. Ohkoshi, S., Ikeda, S., Hozumi, T., Kashiwagi, T. & Hashimoto, K. Photoinduced magnetization with a high Curie temperature and a large coercive field in a cyano-bridged cobalt–tungstate bimetallic assembly. *J. Am. Chem. Soc.* **128,** 5320–5321 (2006).
21. Tokoro, H. *et al.* Visible-light-induced reversible photomagnetism in rubidium manganese hexacyanoferrate. *Chem. Mater.* **20,** 423–428 (2008).
22. Miyano, K., Tanaka, T., Tomioka, Y. & Tokura, Y. Photoinduced insulator-to-metal transition in a perovskite manganite. *Phys. Rev. Lett.* **78,** 4257–4260 (1997).
23. Fiebig, M., Miyano, K., Tomioka, Y. & Tokura, Y. Visualization of the local insulator–metal transition in $Pr_{0.7}Ca_{0.3}MnO_3$. *Science* **280,** 1925–1928 (1998).
24. Åsbrink, S. & Magnéli, A. Crystal structure studies on trititanium pentoxide, Ti_3O_5. *Acta Cryst.* **12,** 575–581 (1959).
25. Hong, S. H. & Åsbrink, S. The structure of γ-Ti_3O_5 at 297 K. *Acta Cryst. B* **38,** 2570–2576 (1982).
26. Onoda, M. Phase transitions of Ti_3O_5. *J. Solid State Chem.* **136,** 67–73 (1998).
27. Chase, M. W. *NIST–JANAF Thermochemical Tables* 4th edn (ed. Chase, M.) Journal of Physical and Chemical Reference Data, Monograph No. 9 (American Chemical Society and American Institute of Physics, 1998).
28. Keys, L. K. & Mulay, L. N. Magnetic susceptibility measurements of rutile and the Magnéli phases of the Ti–O system. *Phys. Rev.* **154,** 453–456 (1967).
29. Bartholomew, R. F. & Frankl, D. R. Electrical properties of some titanium oxide. *Phys. Rev.* **187,** 828–833 (1969).
30. Mulay, L. N. & Danley, W. J. Cooperative magnetic transition in the titanium–oxygen system: a new approach. *J. Appl. Phys.* **41,** 877–879 (1970).
31. Rao, C. N. R., Ramdas, S., Loehman, R. E. & Honing, J. M. Semiconductor–metal transition in Ti_3O_5. *J. Solid State Chem.* **3,** 83–88 (1971).
32. Zachariasen, W. H. Bond lengths in oxygen and halogen compounds of d and f elements. *J. Less-Common Metals* **62,** 1–7 (1978).
33. Kresse, G. & Hafner, J. *Ab initio* molecular dynamics for open-shell transition metals. *Phys. Rev. B* **48,** 13115–13118 (1993).
34. Kresse, G. & Furthmüller, J. Efficient iterative schemes for *ab initio* total-energy calculations using a plane-wave basis set. *Phys. Rev. B* **54,** 11169–11186 (1996).
35. Meinders, E. R., Mijiritskii, A. V., van Pieterson, L. & Wuttig, M. *Optical Data Storage: Phase-Change Media and Recording* (Springer, 2006).
36. Wuttig, M. & Yamada, N. Phase-change materials for rewriteable data storage. *Nature Mater.* **6,** 824–832 (2007).
37. Slichter, C. P. & Drickamer, H. G. Pressure-induced electronic changes in compounds of iron. *J. Chem. Phys.* **56,** 2142–2160 (1972).
38. Izumi, F. & Momma, K. Three-dimensional visualization in powder diffraction. *Solid. State Phenom.* **130,** 15–20 (2007).
39. McHale, J. M., Auroux, A., Perrotta, A. J. & Navrotsky, A. Surface energies and thermodynamic phase stability in nanocrystalline aluminas. *Science* **277,** 788–791 (1997).

40. Ohkoshi, S., Sakurai, S., Jin, J. & Hashimoto, K. The addition effects of alkaline earth ions in the chemical synthesis of ε-Fe_2O_3 nanocrystals that exhibit a huge coercive field. *J. Appl. Phys.* **97,** 10K312 (2005).
41. Makiura, R. *et al.* Size-controlled stabilization of the superionic phase to room temperature in polymer-coated AgI nanoparticles. *Nature Mater.* **8,** 476–480 (2009).

Acknowledgements

This work was performed under the management of the Project to Create Photocatalyst Industry for Recycling-oriented Society supported by the New Energy and Industrial Technology Development Organization. We are grateful to T. Nuida and K. Takeda for drawing the colour figures, K. Tomono for measuring the infrared spectra, Y. Kakegawa, H. Tsunakawa and M. Adachi for collecting TEM images, S. Ohtsuka and T. Moroyama for collecting SEM images, and T. Takasaki, Y. Namatame, M. Saigo and M. Yasaka (Rigaku Corporation) for measuring the XRD patterns. We are thankful for a Grant-in-Aid for the Global COE Program, 'Chemistry Innovation through Cooperation of Science and Engineering' from the Ministry of Education, Culture, Sports, Science and Technology (MEXT), Japan, and the Center for Nano Lithography & Analysis, The University of Tokyo, supported by MEXT, Japan.

Author contributions

S.O. designed and coordinated this study and contributed to all measurements and calculations, and wrote the paper. Y.T. carried out synthesis, DSC and first-principle band calculation. T.M. carried out synthesis. A.N. performed XRD measurements, Rietveld analysis and ICP-MS. F.H. carried out synthesis and TEM, SEM and SQUID measurements. K.H. contributed to the discussion. H.T. carried out synthesis and thermodynamic analysis, and carried out the photoirradiation and pressure-effect experiments. All authors commented on the manuscript.

Additional information

The authors declare no competing financial interests. Supplementary information accompanies this paper at www.nature.com/naturechemistry. Reprints and permission information is available online at http://npg.nature.com/reprintsandpermissions/. Correspondence and requests for materials should be addressed to S.O.